Ore Geology Reviews 72 (2016) 343–354

Contents lists available at ScienceDirect

Ore Geology Reviews

journal homepage: www.elsevier.com/locate/oregeorev

Different proportion of mantle-derived noble gases in the Cu–Fe and Fe skarn deposits: He–Ar isotopic constraint in the Edong district, Eastern China

Guiqing Xie [a,*], Jingwen Mao [a], Wei Li [a], Qiaoqiao Zhu [a], Hanbin Liu [b], Guohao Jia [c], Yanhe Li [a], Junjie Li [b], Jia Zhang [b]

[a] MLR Key Laboratory of Metallogeny and Mineral Assessment, Institute of Mineral Resources, CAGS, Beijing 100037, People's Republic of China
[b] Beijing Research Institute of Uranium Geology, China National Nuclear Corporation, Beijing 100029, People's Republic of China
[c] Institute of Geochemistry, Chinese Academy of Sciences, Guiyang 550002, People's Republic of China

ARTICLE INFO

Article history:
Received 8 April 2015
Received in revised form 4 August 2015
Accepted 6 August 2015
Available online 11 August 2015

Keywords:
Fe skarn deposit
Cu–Fe skarn deposit
He–Ar isotopes
Middle–Lower Yangtze River metallogenic belt

ABSTRACT

Cu and Fe skarns are two economically important types of skarn deposit worldwide, but the critical factors controlling the difference in metal associations remain enigmatic. The Edong ore district, China, presents an excellent opportunity to study the differences between Cu–Fe and Fe skarn deposits. We have measured He–Ar isotopes trapped in fluid released by crushing pyrite and chalcopyrite from four well known Cu–Fe and Fe deposits in the Edong district, Eastern China, with the aim of constraining their different fluid source and then discussing the factors controlling their variations between Cu–Fe and Fe skarns.

He–Ar isotopic compositions are markedly different between the Cu–Fe and Fe skarn deposits in the Edong district. $^{3}He/^{4}He$ ratios in the Cu–Fe deposits are 0.75–1.87 Ra and $^{40}Ar/^{36}Ar$ ratios are 300–472. By contrast, He–Ar isotopic compositions in minerals from the Fe deposits have lower $^{3}He/^{4}He$ and $^{40}Ar/^{36}Ar$ ratios of 0.08–0.93 Ra and 299–361, respectively. These results suggest that noble gas of the Cu–Fe and Fe skarn deposits in the Edong district formed by variable degrees of mixing between a magmatic fluid containing a mantle component, and modified air–saturated water (MASW). Importantly, He–Ar isotope data provide compelling evidence that contrasting fluid sources were involved in the formation of the Cu–Fe and Fe deposits, i.e., mineralizing fluids of the Cu–Fe deposits could have a greater contribution from mantle component, and little involvement of MASW than those of the Fe deposits in the Edong district. This conclusion is consistent with obvious differences in the nature of the intrusions related to mineralization, as well as sulfur isotopic compositions of sulfides in the Cu–Fe and Fe deposits. It is most likely that different proportion of mantle-derived noble gases play an essential role in controlling differences between the Cu–Fe and Fe skarn deposits.

1. Introduction

Cu and Fe skarns are the world's most abundant and largest skarn type deposits, respectively (Meinert et al., 2005), and are also two economically important worldwide, particularly in China where Cu and Fe skarn deposits provide 31% and 57% of the high-grade (>50%) iron ore, respectively (e.g., Zhao et al., 2012a; Zhang et al., 2014). Therefore, many Cu and Fe skarn deposits have been extensively studied and summarizing their common features (see latest review by Meinert et al., 2005). However, surprisingly few papers have focused on differences between Cu and Fe skarn deposits (e.g., Meinert, 1995; Pons et al., 2010), and the differences between these types of deposits need further investigation (Einaudi et al., 1981).

Most Cu and Fe skarn deposits are genetically associated with intermediate to felsic intrusions emplaced within or near carbonate rocks, and these associations are compelling evidence for the dominantly igneous source of Cu and Fe metals (e.g., Einaudi et al., 1981), but critical factors controlling their differences in metal associations between Cu and Fe skarn remain enigmatic. Meinert (1995) systematically compiled major and trace element data for plutons related to skarn deposits worldwide, and noted that plutons associated with calcic Fe and Sn skarns represent two end-members of a magmatic spectrum which encompasses magma source (mantle versus crustal melts) and evolution, and plutons associated with other skarn types appear to follow this trend in the order: Fe, Au, Cu, Zn, W, Mo, and Sn (Meinert et al., 2005). However, radiogenic isotope data were not considered in this

* Corresponding author at: MLR Key Laboratory of Metallogeny and Mineral Assessment, Institute of Mineral Resources, Chinese Academy of Geological Sciences, No.26 Baiwanzhuang Road, Beijing 100037, People's Republic of China.
E-mail address: xieguiqing@cags.ac.cn (G. Xie).

http://dx.doi.org/10.1016/j.oregeorev.2015.08.004
0169-1368/

pioneering study (Meinert, 1995). More recently, integrated studies of geochemistry, Sr–Nd isotopes, and zircon Hf isotopes in the Edong district have indicated that intrusions related to Cu–Fe skarn deposits have a greater contribution of mantle melts than intrusions related Fe skarn deposits (e.g., Xie et al., 2011a, 2015). The geological, geochronological, and mineralogical evidence indicate that the porphyritic quartz monzonite and granite intrusions are spatially, temporally, and genetically related with Fe skarns at Chengchao in the Edong district (Yao et al., 2015). The H–C–O–S stable isotope review of Cu and Fe skarn deposits are consistent with their derivation from dominantly magmatic fluids which have probably exsloved from crystallizing magma systems (e.g., Bowman, 1998; Meinert et al., 2005). Sulfur isotope showed that mineralizing fluids responsible for formation of the Fe deposits acquired some of their S from evaporites, and contained a larger contribution from evaporitic sedimentary rocks as compared with Cu–Fe deposits in the Edong district (e.g., Zhu et al., 2013, 2015; Xie et al., 2015). Therefore, it is becoming increasingly important to clarify whether there are contrasting fluid sources involved in the formation of Cu–Fe and Fe skarn deposits.

Large differences exist between crustal and mantle noble gas isotopic compositions (Turner et al., 1993). He–Ar isotopes of inclusion-trapped fluid have been studied for several decades, and are a powerful tool for tracing fluid sources and mixing process between mantle volatiles and crustal fluids during the formation of metal deposits (e.g., Stuart et al., 1995; Hu et al., 1998a, 1998b, 2004, 2009, 2012; Burnard et al., 1999; Kendrick et al., 2001; Sun et al., 2009; Shen et al., 2013). In this contribution, we have analyzed He–Ar isotopes in four important Cu–Fe and Fe skarn deposits in the Edong district, Middle–Lower Yangtze River metallogenic belt (MLYRB), including the Tonglushan, Tieshan, Chengchao and Zhangfushan skarn deposits (Fig. 2). By comparing these four important skarn deposits, we then use these data to confirm that contrasting sources are involved in the formation of the Cu–Fe and Fe deposits.

2. Geological background

The MLYRB (Fig. 1) is the most important Cu and Fe metallogenic skarn province in China, and is associated with Late Mesozoic igneous rocks that can be grouped into two associations: the Fe-related group and the Cu-related group (Yang et al., 2011a). The polymetallic skarn deposits in the MLYRB can be considered as Fe-dominated, Au-dominated and Cu–Mo systems (Pirajno, 2013). Tectonically, the MLYRB is located on the northern margin of the Yangtze Craton, and along the southeastern margin of the North China Craton and the Dabieshan orogenic belt (Fig. 1). The MLYRB is bounded by the Xiangfan-Guangji Fault (XGF) to the northwest, the regional strike-slip Tancheng-Lujiang Fault (TLF) to the northeast, and the Yangxin-Changzhou Fault (YCF) to the south (Fig. 1). Geophysical evidence indicates that the Yangtze Fracture Zone exists in the MLYRB, and may have been initiated in the Neoproterozoic, and subsequently been reactivated in the Triassic and Jurassic–Cretaceous (c.f., Chang et al., 1991), which resulted in the development of an extensive network of faults and S-style folds.

The MLYRB is characterized by the following three tectono-stratigraphic units: Archean –Proterozoic metamorphic rocks, Cambrian to Early Triassic marine sedimentary rocks, and Middle Triassic to Cretaceous terrigenous clastic and volcanic rocks. The basement rocks comprise Archean to Middle Proterozoic greenschist, phyllite, and slate, which are intercalated with 990–2900 Ma metaspilite and keratophyre (e.g., Chang et al., 1991). Recent studies have shown that unexposed Archean (3.4–2.9 and 2.8–2.5 Ga) components occurred beneath the crust of the MLYRB (e.g., Tang et al., 2012).

The metamorphic basement is unconformably overlain by extensive marine carbonate and clastic rocks during the Cambrian to Triassic time, among which the Carboniferous, Permian and Triassic carbonate rocks and clastic rocks, are the most important host sedimentary successions for the porphyry–skarn Cu polymetallic deposits (e.g., Chang et al., 1991). For example, Cu and Fe skarn deposits are dominantly hosted

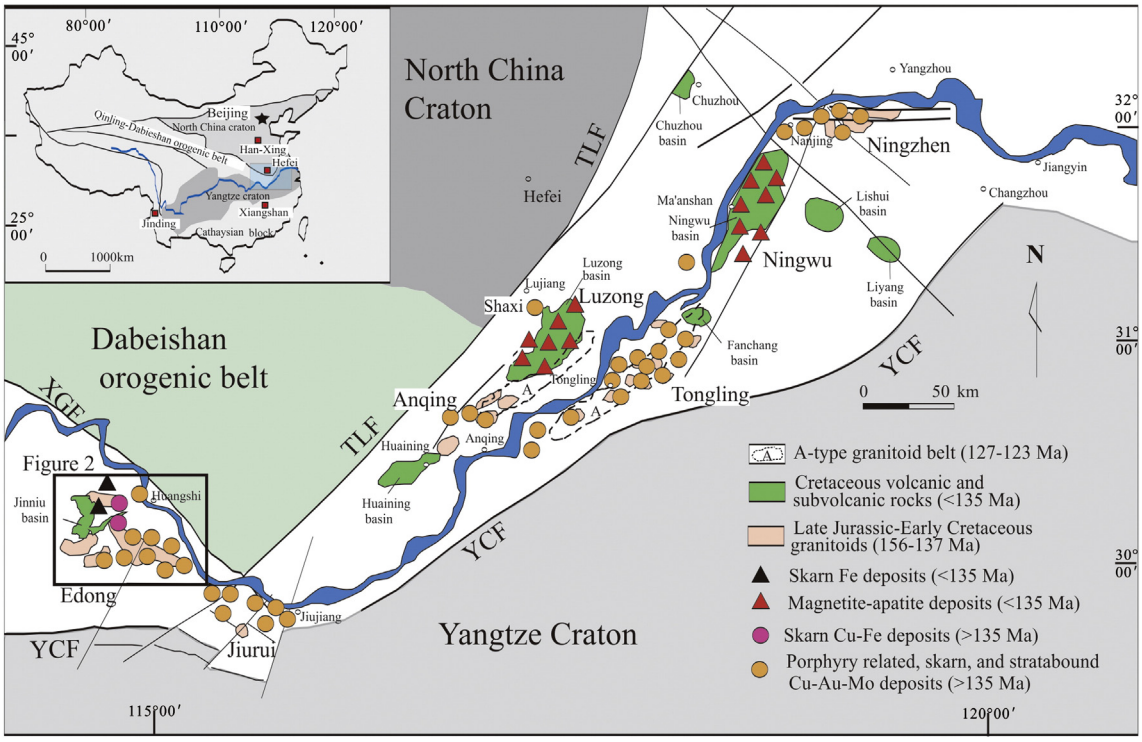

Fig. 1. Sketch map showing the distribution of porphyry related, skarn, and stratabound Cu–Au–Mo–Fe (>135 Ma), magnetite–apatite and Fe skarn deposits (<135 Ma), and Late Mesozoic granitoids and volcano-sedimentary basins along the MLYRB (modified from Mao et al., 2011). TLF: Tancheng – Lujiang Fault, XGF: Xiangfan – Guangji Fault, YCF: Yangxing – Changzhou Fault.

in the Triassic carbonate rocks with intercalating gypsum, accounting for 40% and 90% of total Fe and Cu reserves, respectively, in the Edong district (e.g., Zhai et al., 1992; Pan and Dong, 1999).

Unconformably overlying these sediments is a sequence of Cretaceous volcanic and volcano-clastic rocks, which are primarily welded breccia, tuff, andesite, rhyolite, trachyte, and basalt. Recent integrated geological studies, coupled with zircon U–Pb dating, have provided compelling evidence that Late Jurassic volcanic–sedimentary rocks are absent, and that volcanic rocks in the Jinniu, Luzong, Fanchang, and Ningwu basins (Fig. 1) formed at 125–130, 127–137, 126–134, and 127–135 Ma, respectively (e.g., Zhou et al., 2008a, 2011; Xie et al., 2011b; Chen et al., 2014). Upper Cretaceous to Quaternary rocks is characterized by clastic red-bed sediments intercalated with minor Paleogene basalts (Chang et al., 1991).

The ore deposits and associated igneous rocks in the MLYRB have been extensively studied, and major reviews include Chang et al. (1991), Zhai et al. (1992) and Pan and Dong (1999). Recent articles show that the metallogenic epoch and characteristics in the MLYRB are different from those in the Nanling region, South China (e.g., Hu and Zhou, 2012), and three types with different ages of metallic mineral deposits and associated magmatism have been recognized in the MLYRB (e.g., Zhou et al., 2008b; Mao et al., 2011): (1) 135–148 Ma Cu–Au–Mo–Fe porphyry–skarn–stratabound deposits (including Cu–Fe skarn deposits), associated with 137–156 Ma high-K calc-alkaline granitoids in uplifted areas (Fig. 1); (2) 123–135 Ma magnetite–apatite deposits, associated with 123–135 Ma shoshonitic rocks in Cretaceous volcanic basins (Fig. 1); and (3) a small number of uneconomic Cu–Au hydrothermal veins, associated with 125–127 Ma A-type granitoids and alkaline volcanic rocks. However, there are a few exceptions, such as the important Fe-only skarn deposits in the Edong district (Fig. 1) that are coeval with the magnetite–apatite deposits (Mao et al., 2011). Recently, the metallogenic model of intracontinental porphyry–skarn Cu polymetallic deposits in the MLYRB was discussed and reviewed (Zhou et al., 2015).

The Edong district in southeast Hubei Province is situated in the westernmost part of the MLYRB (Fig. 1). Compared with other districts in the MLYRB (Fig. 1), the Edong ore district is one of the most important Fe and Cu–Fe skarn concentrations in China (e.g., Li et al., 2014). In the southern part of this area, Late Proterozoic metamorphic rocks are poorly exposed, but Cambrian to Middle Triassic marine carbonate rocks, clastic rocks, flysch and minor gypsum successions (>6000 m thick) are widespread, and Late Triassic to Middle Jurassic clastic rocks are locally exposed (c.f., Shu et al., 1992). The western part of the area contains Early Cretaceous volcanic and sedimentary rocks in the Jinniu Basin (Fig. 2), which comprised (from base to top) the Majiashan, Lingxiang and Dasi Formations. The latter is volumetrically dominant and widespread, and consists of rhyolite, basalt, basaltic andesite, trachy–basalt, basaltic trachy–andesite, trachy–andesite, trachy–dacite, and rhyolite (e.g., Xie et al., 2006). Volcanic rocks in the Jinniu Basin have been dated at 125–130 Ma by the SHRIMP zircon U–Pb method (Xie et al., 2011b), and are younger than the quartz diorite and Cu–Fe skarn deposits, which have ages of 137–142 Ma by the SHRIMP and LA–ICPMS zircon U–Pb method (e.g., Li et al., 2009, 2014; Xie et al., 2011c).

In the Edong district, numerous skarn mineral systems are found around the Late Mesozoic intrusions. For example, some Fe deposits are found along the southern contact of the Echeng and Jinshandian plutons, some Fe–Cu deposits are present along the contact of the Tieshan pluton, some Cu–Fe, Au–Cu and Cu deposits occur around the Yangxin pluton, and some Fe–Cu deposits and Au–Cu occurrences occur around the Lingxiang pluton (IMRCAGS, 2005) (Fig. 2). These skarn deposits are located at the intersections of faults and folds that trend NNE–SSW and NW–SE to WNW–ESE, and are hosted along the contacts between Carboniferous to Triassic carbonate rocks and Late Mesozoic intrusions. In addition, there are developed many granitic porphyry stocks, and important Cu–Mo and W–Cu porphyry–skarn deposits (Fig. 2), as in the cases of the Tongshankou Cu–Mo and Ruanjiawan W–Cu deposits (e.g., Xie et al., 2007; Li et al., 2008; Deng et al., 2015). Fe skarns are

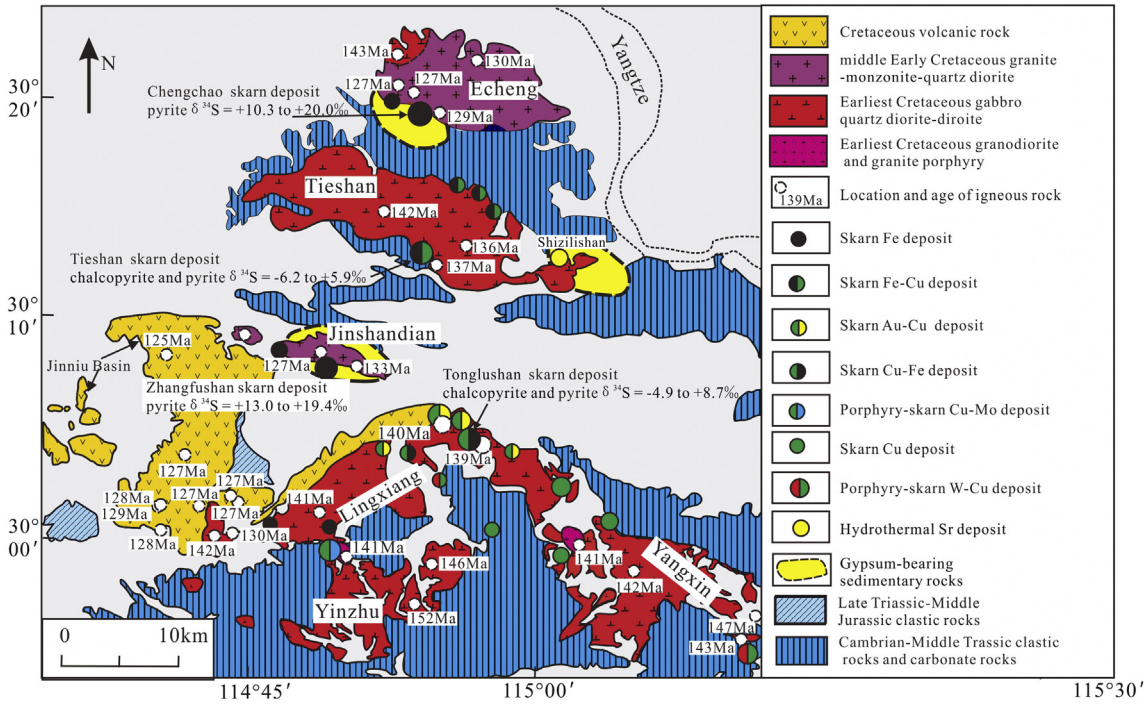

Fig. 2. Geological map of the Edong district in southeast Hubei province, MLYRB, showing the main types of metallic deposits, hydrothermal Sr deposit, and gypsum-bearing sedimentary rocks (modified from Shu et al., 1992), ages of intrusions (Li et al., 2008, 2009; Xie et al., 2011a, 2011b, 2012), and sulfur isotopic data for sulfides and anhydrites from selected Cu–Fe and Fe skarn deposits (Xie et al., 2015 and references therein).

mined for their magnetite contents, and Fe typically is the only commodity recovered in the Fe skarn deposits, but some deposits contain significant amounts of Cu, and are transitional to more typical Cu skarn (e.g., Meinert et al., 2005). As such, the Edong district is ideal for comparative studies of Cu–Fe and Fe skarn deposits. In order to correctly discuss contrasting Cu–Fe and Fe deposits in the Edong district, in this contribution the Fe–Cu and Cu–Fe skarns are hereafter referred to as Cu–Fe skarn deposits for those containing economic concentrations of Cu, while Fe skarn deposits here for those that are mined for their magnetite with uneconomic copper contents, which were also called the Fe-only skarn deposit (Mao et al., 2011).

3. Principal characteristics of the Cu–Fe and Fe skarn deposits

To date, 4 well known Cu–Fe and Fe skarn deposits (i.e. Tieshan, Tonglushan, Chengchao, and Zhangfushan) (Fig. 2) have been discovered along the contact of the Echeng, Jinshandian, Tieshan, and Yangxin plutons (IMRCAGS, 2005). The Fe and Cu–Fe skarn deposits are dominant, and account for 99% of the proven Fe and 57% of the proven Cu reserves in the Edong district (Fig. 2) (e.g., Shu et al., 1992). Detailed summary of these four selected Cu–Fe and Fe deposits in the Edong ore district have been presented by Xie et al. (2015).

Precise radiometric dating of the deposits (e.g., Xie et al., 2007, 2011a, 2011b, 2012; Li et al., 2014; Zhu et al., 2014) has demonstrated that two different types of Fe-bearing skarn mineralization are recognized in this region: (1) 137–148 Ma Cu–Fe deposits, as exemplified by Tonglushan and Tieshan (Fig. 2); and (2) 130–133 Ma Fe deposits, as exemplified by Chengchao and Zhangfushan (Fig. 2). There is considerable variation in the spatial distribution of these deposits. The Cu–Fe deposits are mainly found in the eastern part of the Edong district, whereas the Fe deposits are mainly present in the western part of the district (Fig. 2).

Previous studies have shown that both Cu–Fe and Fe deposits in the Edong district are characterized by dominantly exoskarn and subordinate endoskarn, and that both Cu–Fe and Fe skarn systems share similar garnet and pyroxene compositions, which are predominantly andradite ($Ad_{29-100}Gr_{0-68}$) and diopside ($Di_{54-100}Hd_{0-38}$), respectively (c.f., Xie et al., 2015). However, there are clear differences between the Cu–Fe and Fe skarn deposits in the Edong district. For example, intrusions related to the Cu–Fe deposits are diorite and quartz diorite, whereas those related to the Fe deposits are quartz diorite, granite, and monzonite (e.g., Xie et al., 2012; Yao et al., 2015). The Cu–Fe deposits contain gold as a by-product, as in the cases of Tonglushan (reserves of 1.1 Mt Cu at an average grade of 1.78%, 56.8 Mt Fe ores with an average grade of 41.1%, and 69 t of Au at an average grade of 1.15 g/t), and Tieshan (0.67 Mt of Cu at an average grade of 0.57%, 160 Mt of Fe ores with an average grade of 52.1%, and 48 t Au) (Fig. 2) (c.f., Yao et al., 1993). The Fe deposits like those at Chengchao and Zhangfushan contain neither gold or copper by-products, and contain reserves of 200 Mt of magnetite ore at an average grade of 45.1% Fe, and 128 Mt of Fe ore with an average grade of 42.3%, respectively (Fig. 2) (c.f., Yao et al., 1993; IMRCAGS, 2005). The Cu–Fe deposits have been referred to as being gold-rich Cu and/or Fe skarns in the Early Cretaceous Yangtze gold province (Goldfarb et al., 2014), and exhibit positive correlations between Cu and Au contents in the ore, which is similar to those in the Shaxi porphyry Cu–Au deposits from the Luzong district, MLYRB (Fig. 1) (Yang et al., 2011b), and both are clearly different from the Fe skarn deposits. In addition, the ore-hosting sedimentary rocks are different between these Fe and Cu–Fe deposits (Fig. 3), which might be play an important role in determining the role of evaporites during the formation of these deposits (Xie et al., 2015; Zhu et al., 2015).

4. Analytical methods

Twenty-two sulfide ores from the Cu–Fe and Fe skarn deposits, including Tonglushan, Tieshan, Chengchao, and Zhangfushan (Table 1) were collected from underground workings and drillhole for He and Ar analysis. Pyrite and chalcopyrite are present either as aggregates in anhydrite veins cutting skarn assemblages or as disseminations in massive magnetite ores, which are from the sulfide stage in the formation of these skarn deposits. After the samples were crushed, pyrite or chalcopyrite chips were hand-picked under a binocular microscope, purified to >99% removing silicate inclusions, and then ultrasonically cleaned in alcohol and dried. Approximately 100–1000 mg of coarse-grained (>250 μm) chalcopyrite or pyrite chips were baked at about 120–150 °C in an ultra-high vacuum system for >24 h prior to analysis to remove adhered atmospheric gases.

He and Ar isotopic compositions of inclusion-trapped fluids from six sulfides and two pyrites from the Tonglushan and Tieshan, respectively, and two pyrites (CC375–19 and CC375–10) at Chengchao were measured with an all-metal extraction line and mass spectrometer (GV 5400) at the State Key Laboratory of Ore Deposit Geochemistry, Institute of Geochemistry, Chinese Academy of Sciences, Guiyang, China. The sensitivities of the GV5400 for He and Ar were 3.9725×10^{-4} A/Torr and 1.1018×10^{-3} A/Torr, respectively, and the mass resolution of the high mass faraday and multiplier were 228.1 and 628.3, respectively. The crushing and analytical procedures followed Hu et al. (2012). Gas abundances were measured by peak-height comparison with known amounts of standard air from an air bottle, and the isotopes and abundances of He and Ar were measured with analytical errors of < 10%. Procedural blanks with $< 2 \times 10^{-10}$ cm^3 STP ^4He and $(2–4) \times 10^{-10}$ cm^3 STP ^{40}Ar were insignificant. Five of the 10 samples were crushed twice to test for post-entrapment modification of He–Ar isotopes trapped in fluid inclusions (e.g., Hu et al., 1998a).

The other six pyrites and six pyrites from Chengchao and Zhangfushan, respectively, were analyzed for He and Ar isotopic compositions using an all-metal extraction line coupled mass spectrometer (Helix SFT) at the Analytical Laboratory Beijing Research Institute of Uranium Geology, China National Nuclear Corporation, Beijing, China. The sensitivities of the Helix SFT for He were $>2 \times 10^{-4}$ A/Torr at 800 μA, and for Ar > 7×10^{-4} A/Torr at 200 μA, respectively. The resolution of Faraday is more than 400, and the resolution of the multiplier is superior to 700 which can completely separate ^3He and HD +. The system blank was measured according to the same procedure for the sample analysis but without crushing the sample, and helium and argon blanks were below 2×10^{-11} cm^3 STP and 1×10^{-10} cm^3 STP respectively. Gas abundance was measured by peak–height comparison with known amounts of standard air from an air bottle with $^3He/^4He$ ratio 1.399×10^{-6} and $^{40}Ar/^{36}Ar$ ratio 295.5, and the size of the pipettes of He and Ar is 2516 cm^3 STP. The details of these crushing and analytical methods are described below:

Gas extraction and processing were performed in a 316 stainless steel extraction line. The pyrite chips were loaded into the crusher and baked into the turbo pump at ~150°C for at least 24 h to remove the gas adsorbed on the surface of the samples and the inner wall of the crusher. The samples were crushed by a hydraulic press, and the released gases were first purified for 10 min by a "U" shaped cold finger at −70 °C which was controlled by a mixture of dry -ice and alcohol to remove most of water. The other active gases were adsorbed by four Zr–Al getter pumps (two at room temperature, the other two at 450 °C) for 20 min in total. Argon was frozen into a cold finger with charcoal at −193 °C, and then neon was adsorbed by charcoal at 30 K which was achieved by a cryogenic trap. After purification, helium was admitted to the mass spectrometer and analyzed, and the residual gas was pumped. After He analysis, the parameters for the argon analysis were loaded, waiting for 30 min in order to stabilize magnet field. The cold finger was heated to150 °C for 48 h release the argon and inlet it to mass spectrometer.

The source section is fitted with a Nier type source with high ionization efficiency. The split flight tube minimizes volume in order to increase the sensitivity of the instrument. The collector section includes

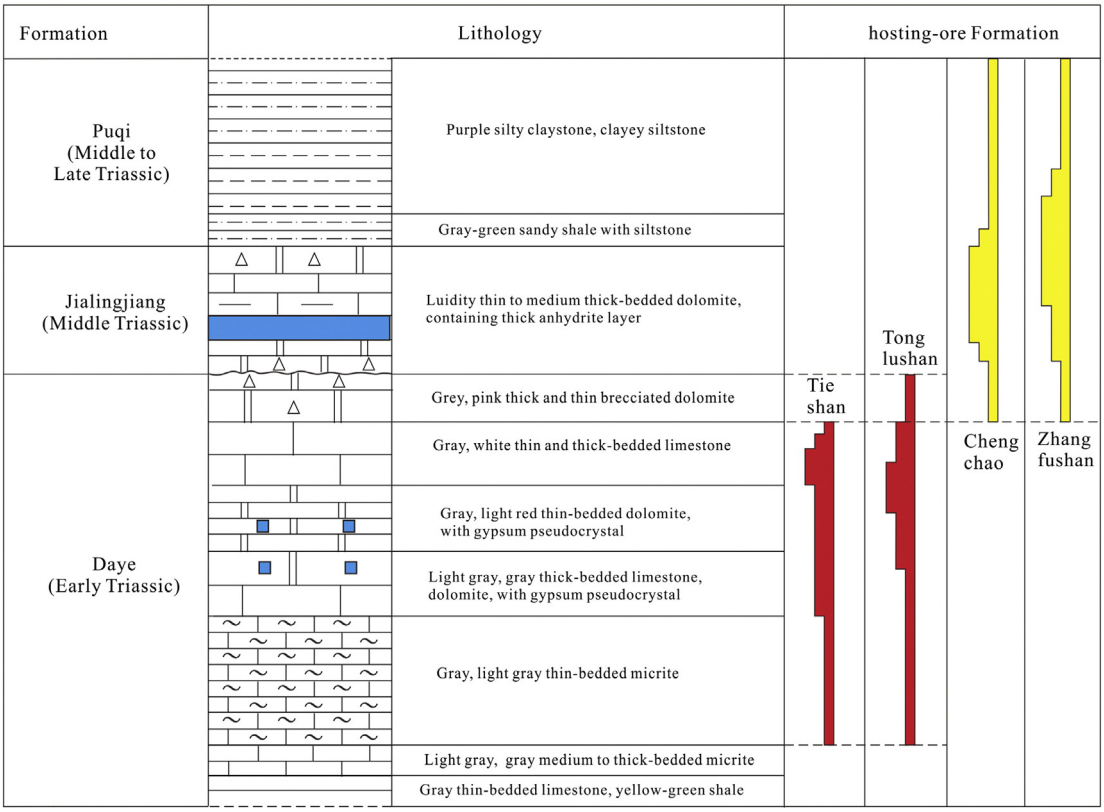

Fig. 3. Triassic lihtostratigraphy of the Edong district, MLYRB, showing the location of ore-hosting sedimentary rocks in the selected Cu–Fe and Fe skarn deposits (modified from Yu et al., 1985; Shu et al., 1992).

a Faraday cup and a multiplier which are able to collect the ^{3}He and ^{4}He simultaneously, and ^{3}He is detected using the multiplier while ^{4}He is measured on the Faraday cup. The Ar isotopes are measured by peak jumping. The choice of the collector for the Ar isotopes measurement depends on the signal of each isotope. The ^{40}Ar is collected on the Faraday cup while the ^{36}Ar and ^{38}Ar are detected using the multiplier. Before the measurement of each sample, the blank of the whole system is measured for background correction, and the standard gases are measured for calibration. The efficiency of the multiplier was often checked to verify the precision of the results.

It is usual that the sample is not 100% crushed. As such, when referring to the content of the gas in the sample, the amount of the sample which was crushed should be taken into consideration. All the gas was extracted from the <100 mesh size fraction (e.g., Burnard et al., 1999).

Table 1
Location and brief description of the samples used for this study from four Cu–Fe and Fe skarn deposits in the Edong district, MLYRB.

Sample Number	Mine	Mineral	Location	Description
TLSB51	Tonglushan	pyrite	−245 m level adit	Cu ore within marble
404 − 29	Tonglushan	pyrite	Drillhole ZK404, 432 m	Sulfide ore within quartz diorite
TLSB99	Tonglushan	chalcopyrite	−365 m level adit	Cu-bearing magnetite ore
TLSB30	Tonglushan	chalcopyrite	−305 m level adit	Sulfide ore within marble
404 − 46	Tonglushan	pyrite	Drillhole ZK404, 216 m	Cu-bearing diopside skarn within quartz diorite
1403 − 25	Tonglushan	pyrite	Drillhole ZK1403, 234 m	Sulfide ore within marble
TSS1	Tieshan	pyrite	Open pit at the Shizishan section	Disseminated sulfide within magnetite and phlogopite skarn
TS74–7	Tieshan	pyrite	−74 m level adit at the Longdong section	Disseminated sulfide within magnetite ore
JS274	Zhangfushan	pyrite	Drillhole ZK4416, 945 m	Disseminated pyrite within magnetite ore
JS318	Zhangfushan	pyrite	Drillhole ZK2818, 1189 m	Pyrite and anhydrite vein within magnetite ore
JS410	Zhangfushan	pyrite	−354 m level adit	Disseminated pyrite within banded magnetite ore
JS456	Zhangfushan	pyrite	Drillhole ZK3417, 646 m	Pyrite, magnetite and calcite vein within hornfels
JS497	Zhangfushan	pyrite	Drillhole ZK3417, 726 m	Pyrite within phlogopite skarn
JS556	Zhangfushan	pyrite	Drillhole ZK127, 774 m	Pyrite within diopside skarn
CC375–10	Chengchao	pyrite	−375 m level adit at western section	Disseminated pyrite within magnetite ore
CC375 − 19	Chengchao	pyrite	−375 m level adit at western section	Disseminated pyrite within magnetite and phlogopite skarn
CC127	Chengchao	pyrite	−430 m level adit at eastern section	Disseminated pyrite and anhydrite within magnetite ore
CC156	Chengchao	pyrite	−430 m level adit at eastern section	Coarse pyrite and anhydrite vein within diopside skarn
CC162	Chengchao	pyrite	−430 m level adit at western section	Disseminated pyrite within massive magnetite ore
CC224	Chengchao	pyrite	Drillhole WK4522, 95 m	Coarse pyrite coexisting with anhydrite
CC182	Chengchao	pyrite	−430 m level adit at western section	Coarse pyrite within massive magnetite ore
CC185	Chengchao	pyrite	Drillhole WK3711, 18 m	Veinlet-coarse pyrite within anhydrite

After crushing, the samples were passed through a 100 mesh sieve and weighed. The content of the gas in the sample was calculated by the fraction which passed through the 100 mesh sieve.

5. Results

Both the density of fluid inclusions in the sample, and the efficiency and processes of in vacuo–crushing affect estimates of the noble gas concentrations in sulfides, therefore noble gas concentrations are semi-quantitative (e.g., Burnard et al., 1999) or have very little geological significance (Kendrick and Burnard, 2013). However, the noble gas isotopic ratios can quantify the presence of mantle and atmospheric components in crust fluids (see latest review by Kendrick and Burnard, 2013). Consequently, He and Ar isotope ratios of fluid inclusions in pyrite and chalcopyrite from the Cu–Fe and Fe deposits are listed in Table 2, and He–Ar concentrations in sulfide are given for reference only in Table 2.

As shown in Fig. 4, He–Ar isotopic compositions are markedly different for the Cu–Fe and Fe skarn deposits, i.e., $^{3}He/^{4}He$ ratios in the Cu–Fe skarns are 1.05–2.60 $\times 10^{-6}$ (0.75–1.87 Ra; Ra = 1.4 $\times 10^{-6}$ and is the $^{3}He/^{4}He$ ratio of air), $^{40}Ar/^{36}Ar$ ratios are 300–472, and $^{3}He/^{36}Ar$ ratios are 0.91–8.48 $\times 10^{-4}$ (Table 2). In contrast, minerals from the Fe deposits have lower He–Ar isotopic compositions, with $^{3}He/^{4}He$, $^{40}Ar/^{36}Ar$, and $^{3}He/^{36}Ar$ ratios of 0.12–1.29 $\times 10^{-6}$ (0.08–0.93 Ra), 299–361, and 0.05–1.61 $\times 10^{-4}$, respectively (Table 2). In addition, the Cu–Fe and Fe skarns share similar $^{40}Ar^{*}/^{4}He$ ratios with 58.5–1261.3 $\times 10^{-3}$ and 81.0–972.2 $\times 10^{-3}$, respectively (Table 2).

6. Discussion

6.1. Reliability of the He–Ar compositions of the ore–forming fluids

Case studies have shown that the He–Ar isotopes can trace the origin of fluids in ancient metallic deposits (e.g., Stuart et al., 1995; Hu et al., 1998a), but the extent of post-trapping modification, including He loss, in situ production of ^{4}He and ^{40}Ar, contamination by atmospheric Ar, and cosmogenic ^{3}He (e.g., Burnard et al., 1999; Ballentine et al., 2002; Hu et al., 2012) must be considered before constraining the origin of the ore-forming fluid. Significant post-trapping modification of He–Ar isotopes in the samples can be ruled out for the following reasons:

(1) The sulfides in this study were collected from sulfide stage ores with no evidence of deformation, and the trapped fluid inclusions in the coexisting anhydrite and quartz with sulfides are predominantly primary (e.g., Shu et al., 1992; Zhao et al., 2012b; Ren et al., 2012). Experimental evidence has shown that $^{3}He/^{4}He$ ratios from trapped hydrothermal fluids in ocean-floor sulfides are indistinguishable from those of contemporary vent fluid (e.g., Turner and Stuart, 1992; Baptiste and Fouquet, 1996; Luders and Niedermann, 2010). It has been established that pyrite and chalcopyrite with inclusion trapped He remains closed on a timescale of 100 Ma (e.g., Turner and Stuart, 1992; Baptiste and Fouquet, 1996). Therefore, He loss from the fluid inclusions is unlikely to have affected our samples given their relatively young age (148–132 Ma) (e.g., Xie et al., 2007, 2012; Li et al., 2014; Zhu et al., 2014).

Table 2
He–Ar noble gas compositions of fluids trapped in sulfide grains from Cu–Fe and Fe skarn deposits in the Edong district, MYRB.

Sample No.	Mineral	Crushing number	$^{4}He(10^{-8}\ cm^{3}/g)$	$^{3}He/^{4}He(10^{-6})$	Ra	$^{40}Ar(10^{-8}\ cm^{3}/g)$	$^{40}Ar/^{36}Ar$	$^{3}He/^{36}Ar(10^{-4})$	$^{40}Ar^{*}/^{4}He(10^{-3})$
Cu–Fe skarn deposits									
TLSB51	Pyrite	1	13.50 ± 0.05	1.43 ± 0.02	1.03 ± 0.01	27.81 ± 0.03	314 ± 9	2.18 ± 0.07	119.8 ± 1.9
TLSB51	Pyrite	2	8.51 ± 0.02	1.45 ± 0.05	1.04 ± 0.04	10.96 ± 0.02	409 ± 28	4.59 ± 0.35	357.2 ± 2.3
TLSB51	Pyrite	Total	22.01 ± 0.05	1.44 ± 0.02	1.03 ± 0.02	38.77 ± 0.03	336 ± 9	2.74 ± 0.09	211.6 ± 1.5
404 − 29	Pyrite	1	14.45 ± 0.03	2.20 ± 0.03	1.59 ± 0.02	17.72 ± 0.02	472 ± 23	8.48 ± 0.43	459.0 ± 1.6
TLSB99	Chalcopyrite	1	14.71 ± 0.05	2.55 ± 0.02	1.84 ± 0.02	28.08 ± 0.07	374 ± 7	5.01 ± 0.11	402.7 ± 4.8
TLSB30	Chalcopyrite	1	15.17 ± 0.07	1.05 ± 0.03	0.75 ± 0.02	21.69 ± 0.01	412 ± 27	3.02 ± 0.21	404.5 ± 2.0
404 − 46	Pyrite	1	19.33 ± 0.02	2.60 ± 0.03	1.87 ± 0.02	25.59 ± 0.02	427 ± 21	8.38 ± 0.42	408.7 ± 1.3
1403 − 25	Pyrite	1	27.59 ± 0.18	1.70 ± 0.02	1.22 ± 0.01	35.53 ± 0.17	392 ± 16	5.18 ± 0.22	318.0 ± 6.5
1403 − 25	Pyrite	2	13.83 ± 0.09	1.78 ± 0.03	1.28 ± 0.02	22.20 ± 0.04	395 ± 10	4.37 ± 0.13	403.9 ± 4.0
1403 − 25	Pyrite	Total	41.41 ± 0.20	1.73 ± 0.02	1.24 ± 0.01	57.73 ± 0.18	393 ± 11	4.87 ± 0.14	346.7 ± 4.6
TSS1	Pyrite	1	5.56 ± 0.04	1.19 ± 0.02	0.86 ± 0.02	22.08 ± 0.02	433 ± 10	1.30 ± 0.04	1261.3 ± 10.5
TSS1	Pyrite	2	8.81 ± 0.06	1.24 ± 0.02	0.89 ± 0.01	23.14 ± 0.01	429 ± 8	2.03 ± 0.05	819.6 ± 6.0
TSS1	Pyrite	Total	14.37 ± 0.08	1.22 ± 0.02	0.88 ± 0.01	45.22 ± 0.02	431 ± 7	1.67 ± 0.03	990.6 ± 5.6
TS74 − 7	Pyrite	1	21.49 ± 0.24	1.27 ± 0.03	0.92 ± 0.02	90.06 ± 0.09	300 ± 4	0.91 ± 0.02	58.5 ± 4.2
TS74 − 7	Pyrite	2	36.36 ± 0.14	1.29 ± 0.03	0.92 ± 0.02	87.78 ± 0.04	308 ± 4	1.64 ± 0.05	95.4 ± 1.0
TS74 − 7	Pyrite	Total	57.85 ± 0.28	1.28 ± 0.02	0.92 ± 0.02	177.84 ± 0.10	304 ± 3	1.27 ± 0.03	81.7 ± 1.7
Fe skarn deposits									
JS274	pyrite	1	0.82 ± 0.01	0.12 ± 0.02	0.08 ± 0.01	6.18 ± 0.04	320 ± 5	0.05 ± 0.01	583.2 ± 8.2
JS318	pyrite	1	0.63 ± 0.01	0.44 ± 0.03	0.31 ± 0.02	4.38 ± 0.01	300 ± 4	0.19 ± 0.02	108.9 ± 2.5
JS410	pyrite	1	0.50 ± 0.01	1.18 ± 0.02	0.85 ± 0.01	2.19 ± 0.03	316 ± 8	0.85 ± 0.05	289.5 ± 1.7
JS456	pyrite	1	4.10 ± 0.04	0.29 ± 0.02	0.21 ± 0.01	15.94 ± 0.42	325 ± 9	0.24 ± 0.02	351.8 ± 4.6
JS497	pyrite	1	0.34 ± 0.01	0.72 ± 0.03	0.52 ± 0.02	4.48 ± 0.06	304 ± 8	0.17 ± 0.01	351.7 ± 3.2
JS556	pyrite	1	1.60 ± 0.03	0.51 ± 0.02	0.37 ± 0.01	6.88 ± 0.06	331 ± 8	0.39 ± 0.02	456.2 ± 2.8
CC375–10	pyrite	1	17.92 ± 0.15	0.43 ± 0.02	0.31 ± 0.01	145.42 ± 0.15	299 ± 8	0.16 ± 0.01	90.4 ± 8.2
CC375–19	pyrite	1	1.68 ± 0.04	1.06 ± 0.06	0.76 ± 0.04	27.64 ± 0.18	314 ± 10	0.20 ± 0.01	972.2 ± 41.9
CC375–19	pyrite	2	2.46 ± 0.01	1.29 ± 0.05	0.93 ± 0.03	23.21 ± 0.04	298 ± 12	0.41 ± 0.02	81.0 ± 6.7
CC375–19	pyrite	Total	4.14 ± 0.01	1.20 ± 0.04	0.86 ± 0.03	50.85 ± 0.07	307 ± 12	0.30 ± 0.01	442.5 ± 17.2
CC127	pyrite	1	0.12 ± 0.01	0.64 ± 0.04	0.46 ± 0.03	0.43 ± 0.01	311 ± 12	0.54 ± 0.03	177.5 ± 3.4
CC156	pyrite	1	1.59 ± 0.02	0.33 ± 0.03	0.24 ± 0.02	1.10 ± 0.03	341 ± 5	1.61 ± 0.11	92.8 ± 1.3
CC162	pyrite	1	0.74 ± 0.01	0.73 ± 0.03	0.52 ± 0.02	1.35 ± 0.04	313 ± 10	1.24 ± 0.07	102.8 ± 1.8
CC224	pyrite	1	0.24 ± 0.01	0.44 ± 0.02	0.31 ± 0.01	1.53 ± 0.05	311 ± 8	0.22 ± 0.01	315.6 ± 5.5
CC182	pyrite	1	0.49 ± 0.01	0.88 ± 0.02	0.63 ± 0.01	1.75 ± 0.04	322 ± 5	0.79 ± 0.05	296.8 ± 3.2
CC185	pyrite	1	0.08 ± 0.01	0.38 ± 0.03	0.27 ± 0.02	0.56 ± 0.02	305 ± 7	0.17 ± 0.01	210.9 ± 4.0

Note: ^{40}He and ^{40}Ar concentrations in sulfide are given for reference only (see text for discussion), $^{40}Ar^{*} = {}^{40}Ar\text{-}295.5^{*}{}^{36}Ar$; $Ra = (^{3}He/^{4}He)_{sample}/1.4 \times 10^{-6}$.

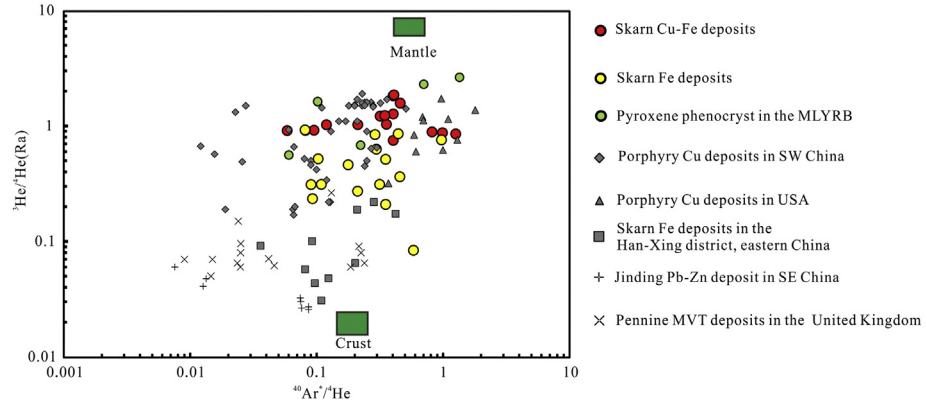

Fig. 4. Plot of $^{3}He/^{4}He$ versus $^{40}Ar^{*}/^{4}He$ for fluid inclusions in sulfides from four selected Cu–Fe and Fe skarn deposits in the Edong district, MLYRB. The fields for crust ($^{3}He/^{4}He = 0.02$ Ra, $^{40}Ar^{*}/^{4}He = 0.2$) and mantle ($^{3}He/^{4}He = 8$ Ra; $^{40}Ar^{*}/^{4}He = 0.69 \pm 0.06$) are from Ballentine et al. (2002). For comparison, shown are He–Ar isotopic compositional fields of porphyry Cu deposits in SW China (Hu et al., 1998a, 2004; Xu et al., 2014a) and USA (Kendrick et al., 2001), skarn Fe deposits in the Han–Xing district, eastern China (Shen et al., 2013), Jinding Pb–Zn deposit in SW China (Hu et al., 1998b), Pennine MVT deposits in the United Kingdom (Stuart and Turner, 1992; Kendrick et al., 2002), and pyroxene phenocrysts from Cenozoic trachybasalts from Hefei in the vicinity of the MLYRB (Xu et al., 2014b).

(2) Compared with data obtained from step heating or fusion techniques, crushing extraction techniques have the advantage that fluid inclusion and matrix noble gas components can be separated to some extent (e.g., Kendrick and Burnard, 2013). As such, measured He–Ar noble gases are preferentially released from fluid inclusions, as opposed to from within the mineral lattice (e.g., Stuart et al., 1994a; Hu et al., 2004, 2012). Radiogenic ^{4}He abundances released from the mineral lattice depend on the grain size of the crushed minerals. The finer grained the mineral becomes with crushing; the larger the surface area of the crushed grains and, therefore, the radiogenic ^{4}He released from the mineral lattice can result in lower $^{3}He/^{4}He$ ratios, which has been documented for some scheelites from the Dae–hwa W–Mo deposit, South Korea (Stuart et al., 1995) and the Pansqueira W–Cu–Sn deposit, central Portugal (Burnard and Polya, 2004). It is not evident in our study that $^{3}He/^{4}He$ ratios decrease with increased crushing (Table 2). Both pyrite and chalcopyrite have extremely low K concentrations (York et al., 1982), suggesting that little in situ ^{40}Ar would be produced from the mineral lattice. Hu et al. (2009) noted that in-situ production of radiogenic ^{4}He is negligible for pyrite-trapped hydrothermal fluid with <0.2 ppm U in the Xiangshan U deposits, east China (Fig. 1). In fact, fluid inclusions trap sufficiently high abundances of noble gases in solution such that in-situ production of radiogenic ^{4}He and ^{40}Ar from dissolved K, U, and Th is only a concern in exceptional circumstances (e.g., Precambrian U deposits) (Kendrick and Burnard, 2013).

(3) Contamination by atmospheric Ar can result in measured $^{40}Ar/^{36}Ar$ ratios being lower than the true $^{40}Ar/^{36}Ar$ ratios of the inclusion-trapped fluids (e.g., Burnard et al., 1999). Although the atmospheric ^{36}Ar absorbed on grain surfaces is impossible to remove completely, it can be overcome by careful sample preparation and using multi-isotope correlations (Kendrick and Burnard, 2013). In our study, when analyzing sample TLSB51, argon became increasingly radiogenic (higher $^{40}Ar/^{36}Ar$) with crushing but $^{3}He/^{4}He$ ratios are constant within error with increased crushing (Table 2), which is most likely due to decreasing contributions from a surface adsorbed atmospheric Ar (e.g., Hu et al., 2012). As such, the only constraint on the true $^{40}Ar/^{36}Ar$ ratios of the inclusion-trapped fluids is that these must have been higher than the highest value measured in our study. Except for sample TLSB51, four other samples including 1403–25, TSS1, TS74-7 and CC375-19 have duplicated relatively well $^{40}Ar/^{36}Ar$ and $^{3}He/^{4}He$ ratios in the first and second crushing (Table 2). Therefore, the $^{40}Ar/^{36}Ar$ variation of different samples in this study may reflect variable $^{40}Ar/^{36}Ar$ of the fluid. Cosmogenic production of ^{3}He cannot have affected our samples, because all samples were collected from underground mines and drillholes (Ballentine and Burnard, 2002).

6.2. He and Ar sources

He–Ar isotopes trapped in fluid inclusions have three potential sources: i.e., air–saturated water (ASW), mantle, and radiogenic isotopes produced within the crust (Turner et al., 1993). However, ASW has too low He abundances to exert a significant influence on He isotopes trapped in most crustal fluids (e.g., Villa, 2001). $^{3}He/^{36}Ar$ ratios with $0.05–8.5 \times 10^{-4}$ measured in this study (Table 2) are obviously higher than those of ASW and the atmosphere with values of 5×10^{-8} and 2×10^{-7}, respectively (Stuart et al., 1995).

Mantle-derived fluid is rich in ^{3}He and poor ^{36}Ar, and has usually high $^{3}He/^{4}He$ (7–9 Ra for most MORB) and $^{40}Ar/^{36}Ar$ (10,000–30,000) ratios (e.g., Ozima and Podosek, 2004). Given the lack of Li–bearing minerals in the Edong district, $^{3}He/^{4}He$ ratios of the crust should be similar to the characteristic crustal values, i.e., $^{3}He/^{4}He < 0.05$ Ra (e.g., Mamyrin and Tolstikhin, 1984). The $^{3}He/^{4}He$ ratios of fluid inclusions can provide a test for evaluating the involvement of mantle-derived fluids in hydrothermal metal ore deposits (e.g., Simmons et al., 1987). The inclusion-trapped He isotopes of sulfides from most crustal fluids with intermediate values of 0.2–2 Ra provide strong evidence for the presence of mantle-derived fluid (Turner et al., 1993). $^{3}He/^{4}He$ ratios of the ore-forming fluids in the Cu–Fe and Fe skarn deposits are higher than those of the crust (<0.05 Ra) (Table 2). It is speculated that these noble gases in the inclusion-trapped fluids in this study were derived from mixtures of two compositionally distinct fluids (i.e., mantle-derived fluid, and crustal fluid with argon from air–saturated water and radiogenic helium produced in the crust). This conclusion is further supported by the variation between He–Ar isotopic ratios (Fig. 5). In this context, the source of He–Ar isotopes identified in our study is comparable to those proposed for other magmatic-hydrothermal metallic deposits (e.g., Stuart et al., 1995; Hu et al., 1998a, 1998b, 2004, 2012; Kendrick et al., 2001; Sun et al., 2009; Shen et al., 2013).

Pure ASW is characterized by atmospheric He and Ar isotopes with $^{3}He/^{4}He = 1.4 \times 10^{-6}$, and $^{40}Ar/^{36}Ar = 298.56 \pm 0.31$ (see latest review by Mark et al., 2011). Radiogenic ^{4}He and ^{40}Ar in aquifer rocks with high lithophile element (U, Th, and K) concentrations will diffuse into groundwater and pore fluids, as such, the crustal fluid trapped in the fluid inclusions might be mixtures of ASW argon and radiogenic

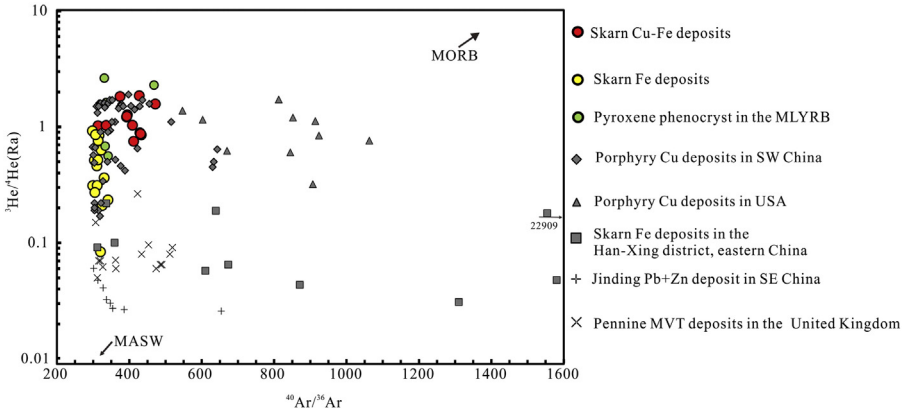

Fig. 5. Plot of $^{3}He/^{4}He$ versus $^{40}Ar/^{36}Ar$ for fluid inclusions in sulfides from four Cu–Fe and Fe skarn deposits in the Edong district, MLYRB. The fields for MASW ($^{3}He/^{4}He = 0.001$ Ra, $^{40}Ar/^{36}Ar = 295.5$) and MORB ($^{3}He/^{4}He = 8$ Ra; $^{40}Ar/^{36}Ar = 10{,}000$) are from Burnard et al. (1999) and Ozima and Podosek (2004), respectively. For comparison, shown are He–Ar isotopic compositional fields of porphyry Cu deposits in SW China and USA, skarn Fe deposits in the Han–Xing district in eastern China, Jinding Pb + Zn deposit in SW China, Pennine MVT deposits in the United Kingdom, and pyroxene phenocrysts from Cenozoic trachybasalts from Hefei in the vicinity of the MLYRB. Data source and symbols are the same as in Fig. 4.

^{4}He and ^{40}Ar (Turner et al., 1993), and characterized by low $^{3}He/^{4}He$ (0.001–0.02 Ra) and $^{3}He/^{36}Ar$ ($<1\times10^{-7}$) ratios, and near-atmospheric $^{40}Ar/^{36}Ar$. This is also known as modified air–saturated water (MASW) (e.g., Burnard et al., 1999; Ballentine et al., 2002; Hu et al., 2004, 2009, 2012).

$^{3}He/^{4}He$ and $^{40}Ar/^{36}Ar$ ratios of the ore-forming fluids of the Cu–Fe and Fe skarn deposits are 0.21–1.87 Ra (except pyrite JS274 = 0.08 Ra), and 299–472, respectively (Table 2). These value are similar to those of porphyry Cu deposits worldwide that have $^{3}He/^{4}He$ = 0.3–2.5 Ra and $^{40}Ar/^{36}Ar$ = 300–3000 (Fig. 5) (c.f., Kendrick and Burnard, 2013), in which ore-forming fluids are considered to have been a mixture between MASW and a magmatic fluid containing a mantle component (e.g., Hu et al., 1998a, 2004; Kendrick et al., 2001; Xu et al., 2014a). Recently, Kendrick and Burnard (2013) pointed out that it is poor practice in the fluid inclusion noble gas literature to use 'mantle' and 'magmatic' almost inter-changeably, and that magmatic fluids in the magmatic-hydrothermal deposits are mostly likely to derived from a mixtures of mantle and crustal gas component (e.g., Hu et al., 1998a, 2004; Ballentine et al., 2002). In addition, $^{3}He/^{4}He$ ratios in the skarn deposits in our study are higher than those of Jinding Pb–Zn deposit in SW China, and Pennine Mississippi Valley-type (MVT) Pb–Zn deposits in the United Kingdom ($^{3}He/^{4}He$ = 0.03–0.26 Ra) (Table 2, Figs. 4–5), which were associated with crustal fluid without involvement of mantle-derived fluid (e.g., Stuart and Turner, 1992; Hu et al., 1999; Kendrick et al., 2002). Therefore, it is clear that the ore-forming fluids of the skarn Cu–Fe and Fe deposits in the Edong district formed by variable degrees of mixing between a magmatic fluid containing a mantle component and MASW, and that mantle-derived fluid was more important in the formation of Cu–Fe deposits than the Fe deposits (see further discussion below). Compare with the skarn Cu–Fe deposits, there is considerable scatter and higher $^{4}He/^{40}Ar$ ratios for the skarn Fe deposits in the Edong district (Fig. 6), indicating addition of crustal–^{4}He fluid in the formation of skarn Fe mineralization (e.g., Burnard et al., 1999), which is similar to other Han-Xing skarn Fe deposits in eastern China and Pennine MVT Pb–Zn deposits in the United Kingdom (e.g., Stuart and Turner, 1992; Shen et al., 2013).

6.3. Contrasting sources between the Cu–Fe and Fe skarn deposits

In most magmatic-hydrothermal ore deposits, He–Ar isotopes of inclusion-trapped fluid are markedly lower than those of MORB (e.g., Kendrick and Burnard, 2013), and may have been affected by two processes: (1) source mixing of radiogenic and mantle-derived noble gases in the magma; and (2) dilution by MASW in the hydrothermal system (e.g., Stuart et al., 1995; Hu et al., 2012). In magma prior to He release into a hydrothermal system, radiogenic helium can be

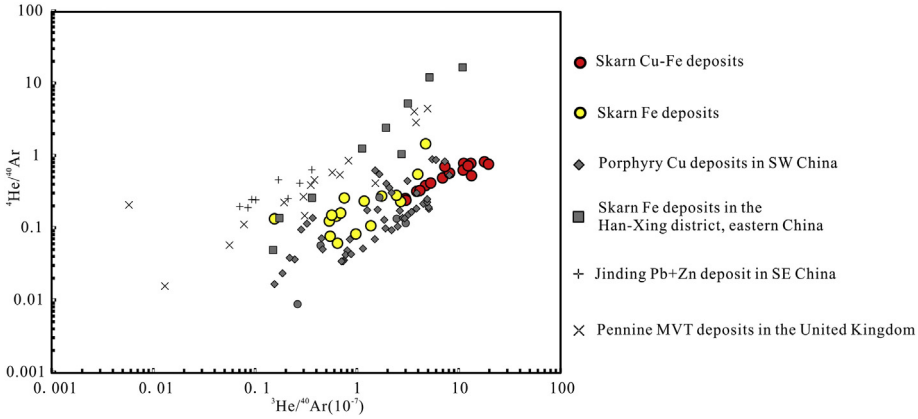

Fig. 6. Plot of $^{4}He/^{40}Ar$ and $^{3}He/^{40}Ar$ for fluid inclusions in sulfides from four Cu–Fe and Fe skarn deposits in the Edong district, MLYRB. For comparison, shown are He–Ar isotopic compositional fields of porphyry Cu deposits in SW China, skarn Fe deposits in the Han–Xing district in eastern China, Jinding Pb + Zn deposit in SW China, and Pennine MVT deposits in the United Kingdom. Data source and symbols are the same as in Fig. 4.

incorporated along with crustal materials and/or "magma aging" where radiogenic helium accumulated due to long residence times (e.g., Simmons et al., 1987; Graham et al., 1988). The He–Ar budget in some continental arcs is dominated by the input of radiogenic He–Ar from the subducting slab, with He–Ar from the mantle wedge making a subordinate contribution to the He-Ar inventory (e.g., Hilton and Porcelli, 2014).

Previous studies have demonstrated that both the Cu–Fe and Fe skarn deposits are spatially and temporally associated with intermediate to felsic intrusions, with the latter derived by partial melting of an enriched lithospheric mantle and variable amounts of lower–crust (e.g., Xie et al., 2008; Li et al., 2009). Previous fluid inclusion and H–O isotope studies indicate that a mixture of dominantly magmatic fluids along with some meteoric fluids was responsible for the formation of Cu–Fe and Fe skarn deposits investigated in this study (e.g., Shu et al., 1992; Ren et al., 2012; Zhao et al., 2012b). As discussed above, the magmatic fluids in this study is likely to have exsolved from parental magmas, which contained a mixture of radiogenic and mantle-derived noble gases. Assimilation of crustal material in the magma chamber may have been the main mechanism for diluting mantle He (e.g., Simmons et al., 1987; Stuart et al., 1995).

Gautheron and Moreira (2002) showed that the helium isotopic ratios are relatively homogenous in continental peridotites and basalts from Europe, USA, Antarctic, Australia and West Africa with a mean ratio of $^3He/^4He$ (6.1 ± 0.9 Ra), but sub-continental lithospheric mantle (SCLM) induced by subducted material were not considered (Gautheron and Moreira, 2002). Although the extents of Paleo-Pacific subduction influence on the MLYRB is highly debated, it is now widely accepted that Phanerozoic SCLM beneath the crust have directly or indirectly affected by subducted materials in the MLYRB (e.g., Mao et al., 2011; Goldfarb et al., 2014; Zhou et al., 2015). The unusual geodynamic setting of the intracontinental porphyry–skarn mineral systems associated with lithospheric thinning and cratonic keel removal in eastern China including MLYRB is the "made-in-China" label (Pirajno and Zhou, 2015). In addition, geophysical studies demonstrated that delamination of the bottom of thick lithospheric mantle in the MLYRB was triggered by asthenospheric upwelling during the Late Mesozoic (e.g., Jiang et al., 2013), which is coincide with the coexistence between fertile and refractory peridotites over a range of depths beneath the crust in the MLYRB as indicated by peridotite xenoliths hosted in the Cenozoic basalts (Lu et al., 2013). Plenty of studies showed there are large variations in the $^3He/^4He$ ratios of SCLM (1.5–20 Ra) (e.g., Moreira, 2013; Hilton and Porcelli, 2014). Recently, pyroxene phenocrysts from Cenozoic continental trachybasalts at Hefei (Fig. 1), in the vicinity of the MLYRB, were derived from enriched SCLM, and are characterized by low $^3He/^4He$ (0.56–2.63 Ra) and air-like $^{40}Ar/^{36}Ar$ (333–469) (Figs. 4–5), and low whole-rock Sr/Y, $(La/Yb)_N$, and εNd(t) values as well as mantle-like ^{18}O values (Xu et al., 2014b). This indicates that the atmospheric Ar and crustal He noble gas components were introduced by subducted crustal-derived melts interacting with mantle wedge peridotite in the MLYRB (Xu et al., 2014b). Considering there is a lack of He–Ar isotope data for Mesozoic mafic rocks in the MLYRB, we speculated that the highest $^3He/^4He$ (2.63 Ra) and $^{40}Ar/^{36}Ar$ (469) of pyroxene in Cenozoic continental trachybasalts from Hefei was assumed to represent the SCLM value for Late Mesozoic skarn deposits in the MLYRB.

As shown in Fig. 5, it is worth noting that the $^{40}Ar/^{36}Ar$ ratios of sulfides in this study overlap with the ratios of the pyroxene phenocrysts in the MLYRB, and similar to those of porphyry Cu deposits worldwide. The cause of generally low $^{40}Ar/^{36}Ar$ ratios of porphyry Cu deposits is debated (e.g., Kendrick and Burnard, 2013), and it is difficult to determine the reason of some MORB glasses with relatively low $^{40}Ar/^{36}Ar$ ratios (<296), including true mantle $^{40}Ar/^{36}Ar$ variation from crustal contamination effects en route, or equilibration with seawater during eruption, or sample vesicularity (Hilton and Porcelli, 2014).

The $^3He/^4He$ ratios (0.93–1.84 Ra) of skarn Cu–Fe deposits are slightly lower than those of SCLM-derived trachybasalts in the vicinity of the MLYRB, but $^{40}Ar/^{36}Ar$ (298–472) and $^{40}Ar^*/^4He$ ($58.5–1261.3 \times 10^{-3}$) ratios of these Cu–Fe deposits are similar to those of the trachybasalts (Figs. 4–5). More recently, a synthesis of sulfur isotopes show that sulfides in the Tonglushan and Tieshan Cu–Fe skarn deposits are characterized by a relatively narrow range of sulfur isotopic composition, with pyrite and chalcopyrite having a range of $\delta^{34}S$ values from −6.2‰ to +8.7‰ with an average of +2.0‰ (n = 118) (Fig. 2) (Xie et al., 2015 and references therein), indicating a predominantly magmatic fluid in the formation of these Cu–Fe deposits.

Previous Sr–Nd isotopic modeling demonstrated that intrusions associated with skarn Cu–Fe deposits in the Edong district were derived by partial melting of enriched lithospheric mantle followed by assimilation of 5–20% of lower-crust (Fig. 7) (Xie et al., 2011a, 2015). Considering the complexity of low $^{40}Ar/^{36}Ar$ ratios in this study (see discussion above), both the binary mixing curves of magmatic fluid and MASW in Fig. 5 and the $^4He/^{40}Ar$–$^3He/^{40}Ar$–$^{36}Ar/^{40}Ar$ three dimensions mixing diagram cannot be shown, and 3-D characterization of He and Ar in ore–deposit systems need further development (Ballentine et al., 2002). Following by the pioneering work of He and Ar containing contributions all three component end-members (mantle, crust, ASW) in deposits (Ballentine et al., 2002), simple modeling of He isotopes of skarn Cu–Fe and Fe deposits in the Edong district is discussed here.

Given that the $^3He/^4He$ ratios of 2.63 Ra, 0.02 Ra, and 0.001 Ra are assumed to represent SCLM He (Xu et al., 2014b), crustal He (e.g., Stuart et al., 1995) and MASW He (e.g., Burnard et al., 1999), respectively, He isotope simple modeling shows that the magmatic fluids (up to 2.11 Ra) emanating from the parental magma in the skarn Cu–Fe deposits were derived from a mixture of mantle-derived magma and assimilation of 20% lower crust before helium was released into the hydrothermal system, and then the maximum value (1.87 Ra) of the Cu–Fe deposits in this study requires 11% MASW and 89% magmatic fluids after the magmatic helium was released into the hydrothermal system. Of course, quantitative modeling on He and Ar isotopes in the Cu–Fe deposits in the Edong ore district is an avenue for future research.

Compared with the Cu–Fe skarn deposits, noble gases trapped in sulfide-hosted fluid inclusions in the Fe skarn deposits have lower $^3He/^4He$ (0.08–0.93 Ra), $^{40}Ar/^{36}Ar$ (299–361) and $^3He/^{36}Ar$ ($0.05–1.61 \times 10^{-4}$) ratios (Figs. 4–5, Table 2). Because neither ^3He nor ^{36}Ar are produced in significant quantities by radioactive processes in the crust (Ballentine and Burnard, 2002), the lower the $^3He/^{36}Ar$ ratio of the inclusion-trapped fluid, the higher the proportion of MASW is (e.g., Hu

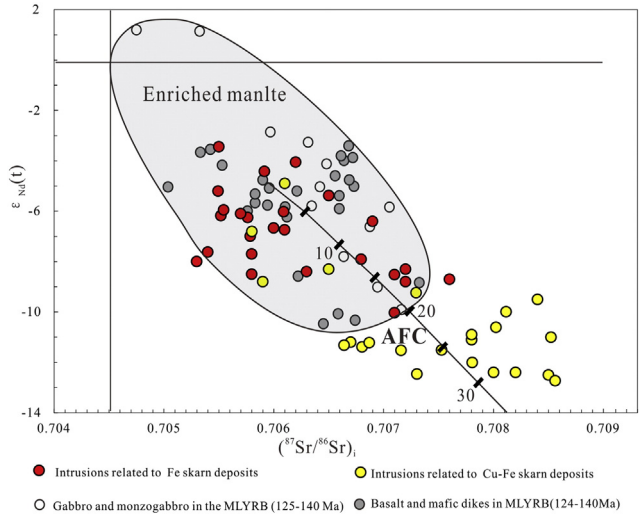

Fig. 7. Nd and Sr isotopic variation diagram for Late Mesozoic intrusions associated with the selected Cu–Fe and Fe skarn deposits in the Edong ore district, MLYRB (Modified from (Xie et al., 2015 and references therein). AFC: assimilation–fractional crystallization.

et al., 2004). This indicates that Fe skarn deposits involved more MASW than skarn Cu–Fe deposits.

Recent Sr–Nd isotopic modeling demonstrated that intrusions associated with the Fe deposits in the Edong district were derived from a mixture of enriched lithospheric mantle melts and a large amount (~35%) of lower-crust (Fig. 7) (Xie et al., 2011a, 2015). Following three component end-members (mantle, crust, ASW) by Ballentine et al. (2002), and given that the $^3He/^4He$ ratios of 2.63 Ra, 0.02 Ra, and 0.001 Ra are assumed to represent SCLM He (Xu et al., 2014b), crustal He (e.g., Stuart et al., 1995) and MASW He (e.g., Burnard et al., 1999), respectively, He isotopes modeling demonstrated that the magmatic fluids (up to 1.72 Ra) in the skarn Fe deposits were derived from a mixture of mantle magma and 35% lower crust before helium was released into the hydrothermal system, and then the maximum value (0.93 Ra) of the Fe deposits in this study requires 54% MASW and 46% magmatic fluids.

Recently, a synthesis of $\delta^{34}S$ values of pyrites in the skarn Fe deposits are +10.3 to +20.0‰, with an average of +16.2‰ (n = 48) (Fig. 2) (Xie et al., 2015 and references therein). Therefore, these Fe deposits have lower $^3He/^4He$ ratios, but heavier S isotopes than the Cu–Fe skarns. The broad negative trend between $^3He/^4He$ and $\delta^{34}S$ in MOR hydrothermal systems of the Northern Juan De Fuca Ridge suggest that sedimentary sulfate and radiogenic He can be added to the hydrothermal fluids and then lower the fluid $^3He/^4He$ ratios in hydrothermal systems (Stuart et al., 1994a, 1994b). Considering the presence of ore-hosting gypsum-bearing sedimentary rocks within the Fe skarn deposits (Figs. 2–3), and larger amount of hydrothermal anhydrite within the ores of the Fe deposits than the Cu–Fe deposits (e.g., Yu et al., 1985; Shu et al., 1992; Yao et al., 1993; Zhu et al., 2013, 2015; Xie et al., 2015), it is speculated here that more radiogenic He and heavier S isotopes of the Fe skarns as compared with the Cu–Fe skarn deposits are genetically associated with incorporation of more sedimentary evaporitic component into the mineralizing fluids.

Above all, He–Ar isotope data provide compelling evidence for different fluid sources in the formation of the Cu–Fe and Fe deposits, with the mineralizing fluids of the Cu–Fe deposits having greater mantle component, and lower MASW as compared with the Fe deposits. This scenario is consistent with previous observation that intrusions associated with the Cu–Fe deposits in the Edong ore district had a greater contribution from the mantle-like melts than in the case of the Fe deposits as suggested by recently published works (e.g., Xie et al., 2011a, 2015).

Recent studies have shown that the contribution of mantle-derived components in ore-forming fluids might positively correlate with the size of porphyry Cu deposits, as reflected by the He–Ar–Os isotopes, i.e., the larger amounts of Cu in the porphyry deposits have lower initial Os ratios and higher $^3He/^4He$ and $^{40}Ar/^{36}Ar$ ratios of the sulfides than the smaller one (e.g., Mathur et al., 2000; Xu et al., 2014a). In contrast, two large Cretaceous skarn Fe deposits from the Han-Xing district in eastern China show relatively lower $^3He/^4He$ (0.04–0.40 Ra) (Figs. 4–5), indicating predominantly deriving from crustal fluids for the formation of the Fe deposits (Shen et al., 2013). If the above observations are correct, then different proportions of mantle component and MASW exert a key influence on the differences between Cu–Fe and Fe skarn deposits.

7. Conclusions

He–Ar isotopic compositions are markedly different between the Cu–Fe and Fe skarn deposits in the Edong district, and noble gas trapped in sulfide-hosted fluid inclusions from the Cu–Fe and Fe deposits in the Edong district are consistent with variable degrees of mixing between a magmatic fluid containing mantle component, and MASW with atmospheric Ar and radiogenic ^4He produced in the crust. Distinct differences between the Cu–Fe and Fe deposits in this study demonstrate that contrasting fluid sources were involved in the formation of the skarn deposits. The mineralizing fluids of the Cu–Fe skarn deposits contained a greater contribution of mantle component, and little MASW than those of the Fe skarn deposits in the Edong district.

Acknowledgments

We thank Hu Qinglu, Jin Shangguang, Wei Ketao, Liu Yucheng, Ke Yufu for providing invaluable assistance during our field investigations. Relevant comments, careful corrections, and constructive suggestions from Professor F.M. Pirajno and two anonymous reviewers greatly improved the quality of the manuscript. This work was supported by the National Basic Research Program of China (973 Program) (2012CB416802), the Basic Scientific Research Operation Cost of State-Leveled Public Welfare Scientific Research Courtyard (K1203), the National Special Research Programs for Non-Profit Trades (Sponsored by MLR, 201311136), the National Science Foundation of China (41372090) and the State Key Laboratory of Ore Deposit Geochemistry, Institute of Geochemistry, Chinese Academy of Sciences, China (201005).

References

Ballentine, C.J., Burnard, P.G., 2002. Production, release and transport of noble gases in the continental crust. Rev. Mineral. Geochem. 47, 481–538.
Ballentine, C.J., Burgess, R., Marty, B., 2002. Tracing fluid origin, transport and interaction in the crust. Rev. Mineral. Geochem. 47, 539–614.
Baptiste, P.J., Fouquet, Y., 1996. Abundance and isotopic composition of helium in hydrothermal sulfides from the East Pacific Rise at 13 N. Geochim. Cosmochim. Acta 60, 87–93.
Bowman, J.R., 1998. Stable isotope sysmatic of skarns. Min. Assoc. Canada Short Course Series 26 pp. 99–145.
Burnard, P.G., Polya, D., 2004. Importance of mantle derived fluids during granite associated hydrothermal circulation: He and Ar isotopes of ore minerals from Panasqueira. Geochim. Cosmochim. Acta 68, 1607–1615.
Burnard, P.G., Hu, R., Turner, G., Bi, X.W., 1999. Mantle, crustal and atmospheric noble gases in Ailaoshan gold deposits, Yunnan Province, China. Geochim. Cosmochim. Acta 63, 1595–1604.
Chang, Y.F., Liu, X.P., Wu, C.Y., 1991. The Copper–iron Belt of the Lower and Middle Reaches of the Changjiang River. Geological Publishing House, Beijing (in Chinese with English abstract).
Chen, L., Zhao, Z.F., Zheng, Y.F., 2014. Origin of andesitic rocks: geochemical constraints from Mesozoic volcanics in the Luzong basin, South China. Lithos 190–191, 220–239.
Deng, X.D., Li, J.W., Zhou, M.F., Zhao, X.F., Yan, D.R., 2015. In-situ LA–ICPMS trace elements and U–Pb analysis of titanite from the Mesozoic Ruanjiawan W–Cu–Mo skarn deposit, Daye district, China. Ore Geol. Rev. 65, 990–1004.
Einaudi, M.T., Meinert, L.D., Newberry, R.J., 1981. Skarn deposits. Econ. Geol. 75thpp. 317–391.
Gautheron, C., Moreira, M., 2002. Helium signature of the subcontinental lithospheric mantle. Earth Planet. Sci. Lett. 199, 39–47.
Goldfarb, R.J., Taylor, R.D., Collins, G.S., Goryachev, N.A., Orlandini, O.F., 2014. Phanerozoic continental growth and gold metallogeny of Asia. Gondwana Res. 25, 48–102.
Graham, D.W., Zindler, A., Kurz, M.D., Jenkins, W.J., Batiza, R., Staudigel, H., 1988. He, Pb, Sr and Nd isotope constraints on magma genesis and mantle heterogeneity beneath young Pacific seamounts. Contrib. Mineral. Petrol. 99, 446–463.
Hilton, D.R., Porcelli, D., 2014. Noble gases as mantle tracers. 2nd ed. Treatise on Geochemistry 3. Elsevier Science, Oxford, pp. 327–353.
Hu, R.Z., Zhou, M.F., 2012. Multiple Mesozoic mineralization events in South China-an introduction to the thematic issue. Mineral. Deposita 47, 579–588.
Hu, R.Z., Burnard, P.G., Turner, G., Bi, X.W., 1998a. Helium and argon systematics in fluid inclusions of Machangqing copper deposit in west Yunnan province, China. Chem. Geol. 146, 55–63.
Hu, R.Z., Zhong, H., Ye, Z.J., Bi, X.W., Turner, G., Burnard, P.G., 1998b. Helium and argon isotope geochemistry of giant Jinding Pb–Zn deposit. Sci. China Ser. D 28, 208–213 (in Chinese).
Hu, R.Z., Bi, X.W., Turner, G., Burnard, P.G., 1999. Helium and argon systematics in ore-bearing fluid of Ailaoshan gold deposit belts, Yunnan Province, China. Sci. China Ser. D 29, 321–330 (in Chinese).
Hu, R.Z., Burnard, P.G., Bi, X.W., Zhou, M.F., Peng, J.T., Su, W.C., Wu, K.X., 2004. Helium and argon isotope geochemistry of alkaline intrusion-associated gold and copper deposits along the Red River–Jingshajiang fault belt, SW China. Chem. Geol. 203, 305–317.
Hu, R.Z., Burnard, P.G., Bi, X.W., Zhou, M.F., Peng, J.T., Su, W.C., Zhao, J.H., 2009. Mantle-derived gaseous components in ore-forming fluids of the Xiangshan uranium deposit, Jiangxi province, China: evidence from He, Ar and C isotopes. Chem. Geol. 266, 86–95.
Hu, R.Z., Bi, X.W., Jiang, G.H., Chen, H.W., Peng, J.T., Qi, Y.Q., Wu, L.Y., Wei, W.F., 2012. Mantle-derived noble gases in ore-forming fluids of the granite-related Yaogangxian tungsten deposit, Southeastern China. Mineral. Deposita 47, 623–632.
Institute of Mineral Resources Chinese Academy of Geological Sciences (IMRCAGS), 2005. Description About Diagram of China's Iron Ore Deposit Resources (Scale of 1:5 Million). Geological Publishing House, Beijing (in Chinese).

Jiang, G.M., Zhang, G.B., Lü, Q.T., Shi, D.N., Xu, Y., 2013. 3D velocity model beneath the Middle–Lower Yangtze River and its implication to the deep geodynamics. Tectonophysics 606, 36–47.
Kendrick, M.A., Burnard, P.G., 2013. Noble Gases and Halogens in Fluid Inclusions: A Journey Through the Earth's Crust. In: Burnard, P.G. (Ed.), The noble gases as geochemical tracers. Springer, Heidelberg, pp. 319–369.
Kendrick, M.A., Burgess, R., Pattrick, R.A.D., Turner, G., 2001. Fluid inclusion noble gas and halogen evidence on the origin of Cu–porphyry mineralising fluids. Geochim. Cosmochim. Acta 65, 2651–2668.
Kendrick, M.A., Burgess, R., Pattrick, R.A.D., Turner, G., 2002. Hydrothermal fluid origins in a fluorite-rich Mississippi Valley-Type District: Combined noble gas (He, Ar, Kr) and halogen (Cl, Br, I) analysis of fluid inclusions from the South Pennine Ore field, United Kingdom. Econ. Geol. 97, 453–469.
Li, J.W., Zhao, X.F., Zhou, M.F., Vasconcelos, P., Ma, C.Q., Deng, X.D., Zhao, Y.X., Wu, G., 2008. Origin of the Tongshankou porphyry–skarn Cu–Mo deposit, eastern Yangtze craton, Eastern China: Geochronological, geochemical, and Sr–Nd–Hf isotopic constraints. Mineral. Deposita 43, 319–336.
Li, J.W., Zhao, X.F., Zhou, M.F., Ma, C.Q., Souza de, Z.S., Vasconcelos, P., 2009. Late Mesozoic magmatism from the Daye region, eastern China: U–Pb ages, petrogenesis, and geodynamic implications. Contrib. Mineral. Petrol. 157, 383–409.
Li, J.W., Vasconcelos, P.M., Zhou, M.F., Deng, X.D., Cohen, B., Bi, S.J., Zhao, X.F., Selby, D., 2014. Longevity of magmatic–hydrothermal systems in the Daye Cu–Fe–Au District, eastern China with implications for mineral exploration. Ore Geol. Rev. 57, 375–392.
Lu, J.G., Zheng, J.P., Griffin, W.L., Yu, C.M., 2013. Petrology and geochemistry of peridotite xenoliths from the Lianshan region: nature and evolution of lithospheric mantle beneath the lower Yangtze block. Gondwana Res. 23, 161–175.
Luders, V., Niedermann, S., 2010. Helium Isotope composition of fluid inclusions hosted in modern submarine hydrothermal systems. Econ. Geol. 105, 443–449.
Mamyrin, B.A., Tolstikhin, I.N., 1984. Helium isotopes in the earth's mantle. Dev. Geochem. 3, 97–134.
Mao, J.W., Xie, G.Q., Duan, C., Pirajno, F., Ishiyama, D., Chen, Y.C., 2011. A tectono-genetic model for porphyry–skarn–stratabound Cu–Au–Mo–Fe and magnetite–apatite deposits along the Middle–Lower Yangtze River Valley, Eastern China. Ore Geol. Rev. 43, 294–314.
Mark, D.F., de Stuart, F.M., Podesta, M., 2011. New high-precision measurements of the isotopic composition of atmospheric argon. Geochim. Cosmochim. Acta 75, 7494–7501.
Mathur, R., Ruiz, J., Munizaga, F., 2000. Relationship between copper tonnage of Chilean base-metal porphyry deposits and Os isotope ratios. Geology 28, 555–558.
Meinert, L.D., 1995. Compositional variation of igneous rocks associated with skarn deposits —chemical evidence for a genetic connection between petrogenesis and mineralization. Min. Assoc. Canada Short Course Series 23, 401–418.
Meinert, L.D., Dipple, G.M., Nicolescu, S., 2005. World skarn deposits. Econ. Geol. 100thpp. 299–336.
Moreira, M., 2013. Noble gas constraints on the origin and evolution of earth's volatiles. Geochem. Perspect. 2, 229–403.
Ozima, M., Podosek, F.A., 2004. Noble Gas Geochemistry. second ed. Cambridge University Press, Cambridge–New York–Melbourne–Madrid–Cape Town.
Pan, Y.M., Dong, P., 1999. The Lower Changjiang (Yangzi/Yangtze River) metallogenic belt, East China: intrusion- and wall rock-hosted Cu–Fe–Au, Mo, Zn, Pb, Ag deposits. Ore Geol. Rev. 15, 177–242.
Pirajno, F., 2013. The Geology and Tectonic Settings of China's Mineral Deposits. Springer, Dordrecht–Heidelberg–London–New York.
Pirajno, F., Zhou, T.F., 2015. Intracontinental porphyry and porphyry–skarn mineral systems in Eastern China: scrutiny of a special case "Made-in-China". Econ. Geol. 110, 603–629.
Pons, J., Franchini, M., Meinert, L.D., López–Escobar, L., Maydagán, L., 2010. Geology, petrography and geochemistry of igneous rocks related to mineralized skarns in the NW Neuquén basin, Argentina: Implications for Cordilleran skarn exploration. Ore Geol. Rev. 38, 37–58.
Ren, Z., Li, J.W., Hu, H., 2012. Fluid inclusion studies of the Chengchao Fe deposit in southeastern Hubei Province, and signification of its genesis. Mineral Deposits 31, 675–676 (supp., in Chinese).
Shen, J., Li, S., Santosh, M., Meng, K., Dong, G., Wang, Y., Yin, N., Ma, G., Yu, H., 2013. He–Ar isotope geochemistry of iron and gold deposits reveals heterogeneous lithospheric destruction in the North China Craton. J. Asian Earth Sci. 78, 237–247.
Shu, Q.A., Chen, P.L., Cheng, J.R., 1992. Geology of Iron–copper Deposits in Eastern Hubei Province, China. Metallurgic Industry Press, Beijing (in Chinese).
Simmons, S.F., Sawkins, F.J., Schlutter, D.J., 1987. Mantle-derived helium in two Peruvian hydrothermal ore deposits. Nature 329, 429–432.
Stuart, F.M., Turner, G., 1992. The abundance and isotopic composition of the noble gases in ancient fluids. Chem. Geol. 101, 97–109.
Stuart, F.M., Turner, G., Duckworth, R.C., Fallick, A.E., 1994a. Helium isotopes as tracers of trapped hydrothermal fluids in ocean–floor sulfides. Geology 22, 823–826.
Stuart, F.M., Duckworth, R.C., Turner, G., Schofield, P.F., 1994b. Helium and sulfur isotopes of sulfide minerals from Middle Valley, Northern Juan De Fuca Ridge. In: Mottl, M.J., Davis, E.E., Fisher, A.T., Slack, J.F. (Eds.), Proceedings of the Ocean Drilling Program Scientific Results 139, pp. 387–392.
Stuart, F.M., Burnard, P.G., Taylor, J.R.P., Turner, G., 1995. Resolving mantle and crustal contributions to ancient hydrothermal fluids: He–Ar isotopes in fluid inclusions from Dae Hwa W–Mo mineralisation, South Korea. Geochim. Cosmochim. Acta 59, 4663–4673.
Sun, X.M., Zhang, Y., Xiong, D.X., Sun, W.D., Shi, G.Y., Zhai, W., Wang, S.W., 2009. Crust and mantle contributions to gold-forming process at the Daping deposit, Ailaoshan gold belt, Yunnan, China. Ore Geol. Rev. 36, 235–249.
Tang, H.Y., Zheng, J.P., Griffin, W.L., Su, Y.P., Yu, C.M., Ren, H.W., 2012. Complex Precambrian crustal evolution beneath the northeastern Yangtze Craton reflected by zircons from Mesozoic volcanic rocks of the Fanchang basin, Anhui Province. Precambrian Res. 220–221, 91–106.
Turner, G., Stuart, F.M., 1992. He/heat ratio and the deposition temperatures of ocean floor sulfides. Nature 357, 581–583.
Turner, G., Burnard, P., Ford, J.L., Gilmour, J.D., Lyon, I.C., Stuart, F.M., Gruszczynski, M., Halliday, A., 1993. Tracing fluid sources and interactions. Philos. Trans. R. Soc. Lond. A 344, 127–140.
Villa, I.M., 2001. Radiogenic isotopes in fluid inclusions. Lithos 55, 115–124.
Xie, G.Q., Mao, J.W., Zhou, S.D., Ye, H.S., Yan, Q.R., Zhang, Z.S., 2006. SHRIMP zircon U–Pb dating for volcanic rocks of the Dasi Formation in southeast Hubei Province, Middle–Lower reaches of the Yangtze River and its implications. Chin. Sci. Bull. 51, 3000–3009.
Xie, G.Q., Mao, J.W., Li, L.R., Qu, W.J., Pirajno, F., Du, A.D., 2007. Re–Os molybdenite and Ar–Ar phlogopite dating of Cu–Fe–Au–Mo (W) deposits in southeastern Hubei, China. Mineral. Petrol. 90, 249–270.
Xie, G.Q., Mao, J.W., Li, L.R., Beirlein, F., 2008. Geochemistry and Nd–Sr isotopic studies of Late Mesozoic granitoids in the southeastern Hubei province, Middle–Lower Yangtze River belt, Eastern China: petrogenesis and tectonic setting. Lithos 104, 216–230.
Xie, G.Q., Mao, J.W., Zhao, H.J., 2011a. Zircon U–Pb geochronological and Hf isotopic constraints on petrogenesis of Late Mesozoic intrusions in the southeast Hubei Province, Middle–Lower Yangtze River belt, East China. Lithos 125, 693–710.
Xie, G.Q., Mao, J.W., Li, X.W., Duan, C., Yao, L., 2011b. Late Mesozoic bimodal volcanic rocks in the Jinniu basin, Middle–Lower Yangtze River Belt (YRB), East China: age, petrogenesis and tectonic implications. Lithos 127, 144–164.
Xie, G.Q., Mao, J.W., Zhao, H.J., Wei, K.T., Jin, S.G., Pan, H.J., Ke, Y.F., 2011c. Timing of skarn deposit formation of the Tonglushan ore district, southeastern Hubei Province, Middle–Lower Yangtze River Valley metallogenic belt and its implications. Ore Geol. Rev. 43, 62–77.
Xie, G.Q., Mao, J.W., Zhao, H.J., Duan, C., Yao, L., 2012. Zircon U–Pb and phlogopite ^{40}Ar–^{39}Ar age of the Chengchao and Jinshandian skarn Fe deposits, Southeast Hubei, Middle–Lower Yangtze River Valley metallogenic belt, China. Mineral. Deposita 47, 633–652.
Xie, G.Q., Mao, J.W., Zhu, Q.Q., Yao, L., Li, Y.H., Li, W., Zhao, H.J., 2015. Geochemical constraints on Cu–Fe and Fe skarn deposits in the Edong district, Middle–Lower Yangtze River metallogenic belt, China. Ore Geol. Rev. 64, 425–444.
Xu, L., Bi, X.W., Hu, R.Z., Tang, Y., Jiang, G., Qi, Y., 2014a. Origin of the ore-forming fluids of the Tongchang porphyry Cu–Mo deposit in the Jinshajiang–Red River alkaline igneous belt, SW China: constraints from He, Ar and S isotopes. J. Asian Earth Sci. 79, 884–894.
Xu, Z., Zheng, Y.F., He, H.Y., Zhao, Z.F., 2014b. Phenocryst He–Ar isotopic and whole-rock geochemical constraints on the origin of crustal components in the mantle source of Cenozoic continental basalt in eastern China. J. Volcanol. Geotherm. Res. 272, 99–110.
Yang, X.Y., Sun, W.D., Zhou, T.F., Deng, J., 2011a. The Middle–Lower Yangtze metallogenic belt. Int. Geol. Rev. 53, 447–448.
Yang, X.Y., Yang, X.M., Zhang, Z.W., Chi, Y.Y., Yu, L.F., Zhang, Q.M., 2011b. A porphyritic copper (gold) ore-forming model for the Shaxi-Changpushan district, Lower Yangtze metallogenic belt, China: geological and geochemical constraints. Int. Geol. Rev. 53, 580–611.
Yao, P.H., Wang, K.N., Du, C.L., Lin, Z.T., Song, X., 1993. Records of China's Iron Ore Deposits. Metallurgic Industry Press, Beijing (in Chinese).
Yao, L., Xie, G.Q., Mao, J.W., Lu, Z.C., Zhao, C.S., Zheng, X.W., Ding, N., 2015. Geological, geochronological, and mineralogical constraints on the genesis of the Chengchao skarn Fe deposit, Edong ore district, Middle–Lower Yangtze River Valley metallogenic belt, eastern China. J. Asian Earth Sci. 101, 68–82.
York, D., Masliwec, A., Kuybida, P., Hanes, J.E., Hall, C.M., Kenyon, W.J., Spooner, E.T.C., Scott, S.D., 1982. $^{40}Ar/^{39}Ar$ dating of pyrite. Nature 300, 52–53.
Yu, Y.C., Li, G., Xiao, G.Q., Yang, H.C., Xue, D.K., Liu, Y.L., 1985. The Tonglushan Cu–Fe skarn deposit. Geological Team of Southeast Hubei Province, Daye (in Chinese).
Zhai, Y.S., Yao, S.Z., Lin, X.D., Zhou, X.N., Wan, T.F., Jin, F.Q., Zhou, Z.G., 1992. Fe–Cu–Au Metallogeny of the Middle–Lower Changjiang Region. Geological Publishing House, Beijing (in Chinese).
Zhang, Z.C., Hou, T., Santosh, M., Li, H.M., Li, J.W., Zhang, Z.H., Song, Z.Y., Wang, M., 2014. Spatio–temporal distribution and tectonic setting of the major iron deposits in China: an overview. Ore Geol. Rev. 57, 247–263.
Zhao, Y.M., Lin, W.W., Bi, C.S., Li, D.X., Jiang, C.J., 2012a. Skarn Deposits of China. Geological Publishing House, Beijing (in Chinese with English abstract).
Zhao, H.J., Xie, G.Q., Wei, K.T., Ke, Y.F., 2012b. Mineral compositions and fluid evolution of the Tonglushan skarn Cu–Fe deposit, SE Hubei, east-central China. Int. Geol. Rev. 54, 737–764.
Zhou, T.F., Fan, Y., Yuan, F., Lu, S.M., Shang, S.G., David, C., Sebastien, M., Zhao, G.C., 2008a. Geochronology of the volcanic rocks in the Luzong (Lujiang–Zongyang) basin and its significance. Sci. China Ser. D 51, 1470–1482.
Zhou, T.F., Fan, Y., Yuan, F., 2008b. Advances on petrogensis and metallogeny study of the mineralization belt of the Middle and Lower Reaches of the Yangtze River area. Acta Petrol. Sin. 24, 1665–1678 (in Chinese with English abstract).
Zhou, T.F., Fan, Y., Yuan, F., Zhang, L.J., Qian, B., Ma, L., Yang, X.F., Cooke, D.R., 2011. Geochronology and significance of volcanic rocks in the Ning–Wu Basin of China. Sci. China Ser. D 54, 185–196.

Zhou, T.F., Wang, S.W., Fan, Y., Yuan, F., Zhang, D.Y., White, N.C., 2015. A review of the intracontinental porphyry deposits in the Middle–Lower Yangtze River Valley metallogenic belt, Eastern China. Ore Geol. Rev. 65, 433–456.

Zhu, Q.Q., Xie, G.Q., Wang, J., Li, W., Yu, B.F., 2013. The relationship between evaporate and ore-forming process of Jinshandian iron skarn deposit. Acta Geol. Sin. 87, 1419–1429 (in Chinese with English abstract).

Zhu, Q.Q., Xie, G.Q., Jiang, Z.S., Sun, J.F., Li, W., 2014. Characteristics and in situ U–Pb dating of hydrothermal titanite by LA–ICPMS of the Jinshandian large iron skarn deposit, Hubei Province. Acta Petrol. Sin. 30, 1322–1338 (in Chinese with English abstract).

Zhu, Q.Q., Xie, G.Q., Mao, J.W., Li, W., Li, Y.H., Wang, J., Zhang, P., 2015. Mineralogical and sulfur isotopic evidence for the incursion of evaporites in the Jinshandian skarn Fe deposit, Edong district, Eastern China. J. Asian Earth Sci. http://dx.doi.org/10.1016/j.jseaes.2015.05.022.